Journal of Computational Physics 539 (2025) 114241

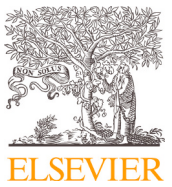

Contents lists available at ScienceDirect

Journal of Computational Physics

journal homepage: www.elsevier.com/locate/jcp

Central-upwind scheme for the phase-transition traffic flow model

Shaoshuai Chu [a], Alexander Kurganov [b,*], Saeed Mohammadian [c], Zuduo Zheng [c]

[a] Department Of Mathematics, RWTH Aachen University, 52056 Aachen, Germany
[b] Department of Mathematics and Shenzhen International Center for Mathematics, Southern University of Science and Technology, Shenzhen, 518055, China
[c] School of Civil Engineering, the University of Queensland, Brisbanev Qld, 4072, Australia

ARTICLE INFO

2020 MSC:
76M12
65M08
76A30
76T99
35L65

Keywords:
Phase-transition traffic flow model
Free traffic flow
Congested traffic flow
Finite-volume methods
Central-upwind schemes

ABSTRACT

Phase-transition models are an important family of non-equilibrium continuum traffic flow models, offering properties like replicating complex traffic phenomena, maintaining anisotropy, and promising potentials for accommodating automated vehicles. However, their complex mathematical characteristics such as discontinuous solution domains, pose numerical challenges and limit their exploration in traffic flow theory. This paper focuses on developing a robust and accurate numerical method for phase-transition traffic flow models: We propose a second-order semi-discrete central-upwind scheme specifically designed for phase-transition models. This novel scheme incorporates the projection onto appropriate flow domains, ensuring enhanced handling of discontinuities and maintaining physical consistency and accuracy. We demonstrate the efficacy of the proposed scheme through extensive and challenging numerical tests, showcasing their potential to facilitate further research and application in phase-transition traffic flow modeling. The ability of phase-transition models to embed the "time-gap"—a crucial element in automated traffic control—as a conserved variable aligns seamlessly with the control logic of automated vehicles, presenting significant potential for future applications, and the proposed numerical scheme now substantially facilitates exploring such potentials.

1. Introduction

Continuum models treat traffic flow as a compressible fluid and analyze its dynamics using aggregated state variables like flow and density, proving beneficial in real-world traffic management and control [1]. Over time, a variety of continuum models have been developed, each incorporating different empirical and behavioral characteristics of traffic flow; see, e.g., the recent works in [2–6]. These models are generally classified into two main categories: equilibrium and non-equilibrium models. Equilibrium models are based on flow conservation principles, consistently linking speed and density without time or space differentiation. In contrast, non-equilibrium models use separate dynamic partial differential equations for speed and density, with their universal relationship only applicable in steady-state equilibrium, irrespective of time and space.

Non-equilibrium continuum traffic flow models are crucial for analyzing traffic dynamics, including the development and spread of persistent waves from initial disturbances to near-equilibrium conditions. To be well-defined, these models must meet the following three criteria:

* Corresponding author.
E-mail addresses: chu@igpm.rwth-aachen.de (S. Chu), alexander@sustech.edu.cn (A. Kurganov), s.mohammadian@uq.edu.au (S. Mohammadian), zuduo.zheng@uq.edu.au (Z. Zheng).

https://doi.org/10.1016/j.jcp.2025.114241
Received 30 December 2024; Received in revised form 29 June 2025; Accepted 13 July 2025
Available online 16 July 2025

- Adherence to causality laws, implying that drivers respond to stimuli ahead of them, and thus, characteristic traffic waves, generated by the model, must not exceed average traffic speeds due to this directional response [7];
- Considering the fact that the negative correlation between driver speed and intervehicular spacing restricts macroscopic traffic conditions between specific paths on the flow-density diagram, the model must ensure that traffic states stay within these viable trajectories and automatically satisfy the consistency conditions such as zero speed at maximum density [8];
- Distinct representation of the dynamics in free-flow and congested phases, ensuring that phenomena unique to each phase are accurately simulated and exclusive to that phase [9].

To the best of our knowledge, phase-transition models of traffic flow, initially proposed in [10] and further developed in [11,12], represent the only class of non-equilibrium models that endogenously meet all of the aforementioned three criteria. The models in this family consider distinct hyperbolic equations for the free-flow and congestion phases, respectively. In the free-flow phase, a simplified equilibrium model with traffic speed being a direct function of density is used, while for the congestion phase, a 2×2 hyperbolic system is employed, linking the density and speed through a conserved variable, which is equivalent to the inverse of the average time gap.

The phase-transition models are promising from a physical perspective in several regards. An empirical study comparing empirical vehicle trajectories has demonstrated the efficacy of phase-transition models in replicating various complex traffic phenomena, including traffic hysteresis and the convective propagation of congested states [13]. Furthermore, phase-transition traffic flow models introduced in [14] and [11] are excellent foundational models for extension to accommodate the governing principles of Connected and Automated Vehicles (CAVs). This suitability stems from the fact that the time gap, an essential decision variable used in the control laws of CAVs, is already directly incorporated as a conserved variable in these models.

Nevertheless, the significant potential of phase transition models has been overlooked in the traffic flow theory literature, especially concerning numerical simulations and analysis. This research gap can be attributed to the inherent mathematical complexity of these models, which makes them very challenging to simulate numerically using the existing numerical schemes. We can only refer the reader to [15], where a Godunov-type method for a phase-transition model was proposed. In this method, mesh cells along phase boundaries are adjusted for accurate projections and a Glimm-type sampling technique post-projection is employed to preserve the numerical solution's integrity. We stress that the Godunov scheme and other Godunov-type upwind schemes rely on (approximately) solving the (generalized) Riemann problems arising at each cell interface. This introduces significant complexity, primarily due to extensive conditional logic for determining the nature of the solution—shock waves, rarefaction waves, or contact discontinuities—based on local conditions. This detailed case-by-case approach significantly increases computational complexity and overhead, rendering Godunov-type upwind schemes less practical for large-scale applications.

This paper aims to bridge the aforementioned research gap by developing a numerical scheme that overcomes the aforementioned difficulties. The contributions of this study are two-fold. First, we aim to develop a novel, accurate, and robust numerical scheme and demonstrate its performance in solving the Riemann problems across a comprehensive range of challenging scenarios. Second, we utilize the proposed scheme to shed light on the phase-transition model's behavior in a wide range of physically tangible real-world traffic scenarios.

The proposed numerical scheme is based on further development of the second-order semi-discrete central-upwind (CU) schemes, which were introduced in [16–18] (see also [19–21] for recent low-dissipation modifications of the CU schemes) as a "black-box" solver for general hyperbolic systems of conservation laws. In this paper, we incorporate novel mechanisms to tailor the CU scheme for phase-transition models, ensuring physical consistency and accuracy by projecting computed results onto the correct flow domains. To demonstrate the performance of the proposed scheme, extensive and challenging numerical tests are conducted. Furthermore, after sufficiently demonstrating the scheme's performance for Riemann problems, we implement the phase-transition traffic flow model in several complex scenarios, aiming to elaborate on the physical interpretation of the proposed model.

The rest of the paper is organized as follows. In Section 2, we describe the phase-transition traffic flow model. In Section 3, we introduce the designed numerical method for the studied model. Finally, in Section 4, we apply the developed scheme to a number of numerical examples. We demonstrate that the proposed scheme can capture the solution sharply and in a non-oscillatory manner.

2. Phase-transition traffic flow model

The phase-transition model, which was initially proposed in [10] (see also [12,14]), couples two different traffic flow models. In the free-flow domain, where the traffic density ρ is smaller than a given threshold $\rho^f_{\rm cr}$, the following scalar equation for ρ is used:

$$\rho_t+(\rho V_f(\rho))_x=0, \tag{2.1}$$

where V_f is the traffic speed in free flow. In the congested-flow domain, where $\rho>\rho^f_{\rm cr}$, the following second-order traffic flow model is utilized:

$$\begin{cases}\rho_t+(\rho V_c(\rho,q))_x=0,\\ q_t+((q-q^*)V_c(\rho,q))_x=0,\end{cases} \tag{2.2}$$

where V_c is the traffic speed in congested regions. In Eqs. (2.1) and (2.2), x is the spatial variable, t is time, q is a flow-type variable equal to the inverse of drivers' average time gap, and q^* is a constant parameter (we define the corresponding time gap derived from q^* as the equilibrium time gap). Note that q should not be confused with the traffic flow rate, which is obtained as ρV_f in free flow

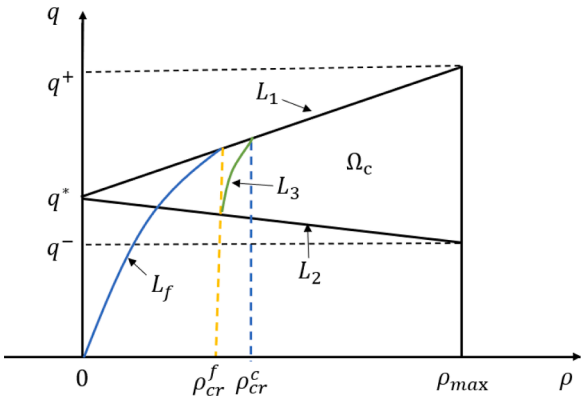

Fig. 2.1. (ρ, q)-diagram of the phase-transition traffic flow model.

and ρV_c in congestion. The functions V_f and V_c are given by

$$V_f(\rho) = V_{\max}, \quad V_c(\rho, q) = \left(1 - \frac{\rho}{\rho_{\max}}\right)\frac{q}{\rho} \tag{2.3}$$

with $V_{\max}$ and $\rho_{\max}$ being the maximum speed and density.

We notice that q is neither defined nor used in Eq. (2.1), but in order to treat the model transition regions, we need to introduce q in the free-flow domain. This is done by substituting $V_c(\rho, q) = V_{\max}$ into Eq. (2.3), which results in

$$q(\rho) = \frac{V_{\max}}{\frac{1}{\rho} - \frac{1}{\rho_{\max}}}. \tag{2.4}$$

In Fig. 2.1, we illustrate the phase transition traffic flow model in the (ρ, q)-plane. The figure divides the plane into two distinct domains: the *free-flow curve* L_f and the *congested-flow domain* Ω_c:

- The free-flow curve L_f is valid for $\rho \in [0, \rho^f_{\rm cr}]$ and represents traffic conditions, in which the vehicles travel at maximum speed without interaction;
- The congested-flow domain Ω_c is bounded by the vertical line $\rho = \rho_{\max}$ and the curves

$$L_1 : \ q = q^* + \frac{q^+ - q^*}{\rho_{\max}}\rho, \quad L_2 : \ q = q^* + \frac{q^- - q^*}{\rho_{\max}}\rho, \quad \text{and} \quad L_3 : \ q = \frac{\rho\rho_{\max}}{\rho_{\max} - \rho}V_{c+}, \tag{2.5}$$

which represent different constraints on the traffic flux under high-density conditions. In Eq. (2.5), $q^{\pm}$ are the maximum/minimum admissible values of q and V_{c+} is the maximum speed in congested domain. Note that the line L_1 and the curve L_3 intersect at the point with

$$\rho = \rho^c_{\rm cr} := \frac{2\rho_{\max}q^*}{\rho_{\max}V_{c+} + 2q^* - q^+ + \sqrt{(\rho_{\max}V_{c+} + 2q^* - q^+)^2 + 4(q^+ - q^*)q^*}}.$$

We stress that the phase transition occurs only along the boundaries between the free and congested domains, specifically near the critical point $\rho = \rho^f_{\rm cr}$, which marks the threshold at which the flow shifts between free and congested states depending on the surrounding traffic conditions. As it was shown in [14], once a solution enters either the free or congested region, it remains there unless it reaches a transition boundary. Therefore, Fig. 2.1 not only presents the structural partitioning of the (ρ, q)-plane but also illustrates the allowed directions and constraints of phase transitions in traffic dynamics.

The studied system Eqs. (2.1)–(2.3) can be put into the following vector form:

$$\boldsymbol{U}_t + \boldsymbol{F}(\boldsymbol{U})_x = \boldsymbol{0}, \tag{2.6}$$

where

$$\boldsymbol{U} = \begin{pmatrix}\rho\\ q\end{pmatrix} \quad \text{and} \quad F(\boldsymbol{U}) = \begin{cases}(\rho V_{\max}, qV_{\max})^\top & \text{if } (\rho, q) \in L_f,\\ (\rho V_c, (q - q^*)V_c)^\top & \text{if } (\rho, q) \in \Omega_c.\end{cases} \tag{2.7}$$

We stress that for the free-flow domain, the equation for q will not be numerically solved, but the vector form Eqs. (2.6)–(2.7) will be convenient for the presentation of the numerical method in the next section.

3. Numerical method

In this section, we develop a second-order semi-discrete CU scheme for the studied phase-transition traffic flow model.

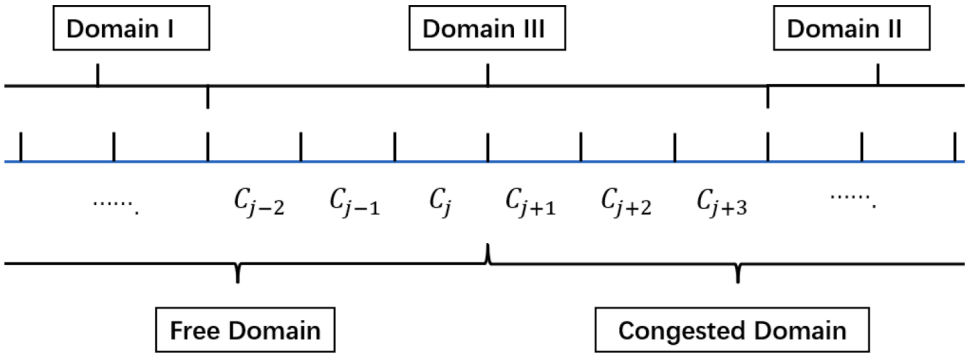

Fig. 3.1. Domains I, II, and III of the phase-transition traffic flow model.

We cover the computational domain with the uniform cells $C_j := [x_{j-\frac{1}{2}}, x_{j+\frac{1}{2}}]$ of size Δx centered at $x_j = (x_{j-\frac{1}{2}} + x_{j+\frac{1}{2}})/2$ and denote by $\overline{\boldsymbol{U}}_j(t)$ the computed cell averages

$$\overline{\boldsymbol{U}}_j(t) :\approx \frac{1}{\Delta x}\int\limits_{C_j} \boldsymbol{U}(x,t)\,\mathrm{d}x. \tag{3.1}$$

We suppose that at a certain time $t \geq 0$, the cell averages $\overline{\boldsymbol{U}}_j(t)$ are available and they all belong to either L_f or Ω_c; see Fig. 2.1. Note that $\overline{\boldsymbol{U}}_j$ and many other indexed quantities, which will be introduced below, are time-dependent and from here on we will suppress this dependence for the sake of brevity.

In the semi-discrete framework, the numerical solution of Eqs. (2.6) and (2.7) is evolved in time by solving the following system of ordinary differential equations (ODEs):

$$\frac{\mathrm{d}\overline{\boldsymbol{U}}_j}{\mathrm{d}t} = -\frac{\boldsymbol{\mathcal{F}}_{j+\frac{1}{2}} - \boldsymbol{\mathcal{F}}_{j-\frac{1}{2}}}{\Delta x}, \tag{3.2}$$

where the CU numerical flux $\boldsymbol{\mathcal{F}}_{j+\frac{1}{2}}$ is given by [17]

$$\boldsymbol{\mathcal{F}}_{j+\frac{1}{2}} = \frac{a^+_{j+\frac{1}{2}}\boldsymbol{F}(\boldsymbol{U}^-_{j+\frac{1}{2}}) - a^-_{j+\frac{1}{2}}\boldsymbol{F}(\boldsymbol{U}^+_{j+\frac{1}{2}})}{a^+_{j+\frac{1}{2}} - a^-_{j+\frac{1}{2}}} + \frac{a^+_{j+\frac{1}{2}}a^-_{j+\frac{1}{2}}}{a^+_{j+\frac{1}{2}} - a^-_{j+\frac{1}{2}}}\left(\boldsymbol{U}^+_{j+\frac{1}{2}} - \boldsymbol{U}^-_{j+\frac{1}{2}} - \boldsymbol{Q}_{j+\frac{1}{2}}\right). \tag{3.3}$$

Here, $\boldsymbol{U}^{\pm}_{j+\frac{1}{2}}$ are the right- and left-sided point values of $\boldsymbol{U}$ at the cell interface $x = x_{j+\frac{1}{2}}$ obtained with the help of a conservative, second-order accurate, and non-oscillatory piecewise linear reconstruction.

We use different reconstructions in the free domain away from the phase-transition areas (Domain I), in the congested domain away from the phase-transition areas (Domain II), and in the phase-transition areas consisting of the six cells (three on the left and three on the right) around each interface between the free- and congested-flow domains (Domain III); see Fig. 3.1.

In Domain I, we only need to compute the one-sided point values $\rho^{\pm}_{j+\frac{1}{2}}$. To this end, we apply the generalized minmod reconstruction (see Appendix A) to the density ρ with $\theta = 1.5$ in Eq. (A.3). In Domain III, we reconstruct both $\rho^{\pm}_{j+\frac{1}{2}}$ and $q^{\pm}_{j+\frac{1}{2}}$ using the same minmod limiter from Appendix A but with $\theta = 1$ in Eq. (A.3) now applied to both ρ and q. Note that here we use a smaller value of θ to minimize possible oscillations in the interface areas. In Domain II, applying the minmod limiter to the ρ- and q-component of the computed solution may lead to relatively large oscillations. In order to suppress them, we apply the minmod limiter with $\theta = 1.5$ in Eq. (A.3) to the local characteristic variables, which are obtained using the local characteristic decomposition (see, e.g., [22–25] and references therein); see Appendix B for details.

Remark 1. We detect the interface using the following simple approach: if $(\bar{\rho}_J - \rho^f_{\mathrm{cr}})(\bar{\rho}_{J+1} - \rho^f_{\mathrm{cr}}) \leq 0$, then $x = x_{J+\frac{1}{2}}$ is the interface, and cells $C_{J-2}, \ldots, C_{J+3}$ belong to Domain III.

After reconstructing the point values $(\rho^{\pm}_{j+\frac{1}{2}}, q^{\pm}_{j+\frac{1}{2}})$, we modify them unless $(\rho^{\pm}_{j+\frac{1}{2}}, q^{\pm}_{j+\frac{1}{2}}) \in L_f$ or $(\rho^{\pm}_{j+\frac{1}{2}}, q^{\pm}_{j+\frac{1}{2}}) \in \Omega_c$. The details on the proposed modification (projection) onto L_f/Ω_c can be founded in Appendix 3.1.

In Eq. (3.3), $a^{\pm}_{j+\frac{1}{2}}$ are the one-sided local speeds of propagation, which can be estimated using the largest (λ_2) and the smallest (λ_1) eigenvalues of the Jacobian $A = \frac{\partial \boldsymbol{F}}{\partial \boldsymbol{U}}$. This can be done as follows (see, e.g., [16,17]):

$$a^+_{j+\frac{1}{2}} = \max\left\{\lambda_2\big(\boldsymbol{U}^-_{j+\frac{1}{2}}\big), \lambda_2\big(\boldsymbol{U}^+_{j+\frac{1}{2}}\big), 0\right\}, \quad a^-_{j+\frac{1}{2}} = \min\left\{\lambda_1\big(\boldsymbol{U}^-_{j+\frac{1}{2}}\big), \lambda_1\big(\boldsymbol{U}^+_{j+\frac{1}{2}}\big), 0\right\}. \tag{3.4}$$

Computing $a^{\pm}_{j+\frac{1}{2}}$ according to Eq. (3.4) requires, however, considering four possible cases depending on whether the left and right reconstructed states $\boldsymbol{U}^{\pm}_{j+\frac{1}{2}}$ are in free or congested domain as in the free-flow domain the eigenvalues of

$$A=\begin{pmatrix} V_{\max} & 0 \\ 0 & V_{\max} \end{pmatrix} \tag{3.5}$$

are $\lambda^f_1=\lambda^f_2=V_{\max}$ and in the congested-flow domain, the eigenvalues of

$$A=\begin{pmatrix} -\dfrac{q}{\rho_{\max}} & \dfrac{\rho_{\max}-\rho}{\rho_{\max}} \\ \dfrac{q(q^*-q)}{\rho^2} & \dfrac{(q^*-2q)(\rho-\rho_{\max})}{\rho\rho_{\max}} \end{pmatrix} \tag{3.6}$$

are

$$\lambda^c_1=(q-q^*)\Big(\frac{1}{\rho}-\frac{2}{\rho_{\max}}\Big)-\frac{q^*}{\rho_{\max}},\quad \lambda^c_2=V_c(\rho,q). \tag{3.7}$$

We then obtain:

- If $(\rho^-_{j+\frac{1}{2}},q^-_{j+\frac{1}{2}})\in\Omega_c$ and $(\rho^+_{j+\frac{1}{2}},q^+_{j+\frac{1}{2}})\in\Omega_c$, we take

$$a^+_{j+\frac{1}{2}}=\max\Big\{\lambda^c_2\big(\boldsymbol{U}^-_{j+\frac{1}{2}}\big),\lambda^c_2\big(\boldsymbol{U}^+_{j+\frac{1}{2}}\big),0\Big\},\quad a^-_{j+\frac{1}{2}}=\min\Big\{\lambda^c_1\big(\boldsymbol{U}^-_{j+\frac{1}{2}}\big),\lambda^c_1\big(\boldsymbol{U}^+_{j+\frac{1}{2}}\big),0\Big\}; \tag{3.8}$$

- If both $(\rho^-_{j+\frac{1}{2}},q^-_{j+\frac{1}{2}})\in L_f$ and $(\rho^+_{j+\frac{1}{2}},q^+_{j+\frac{1}{2}})\in L_f$, we take

$$a^+_{j+\frac{1}{2}}=V_{\max},\quad a^-_{j+\frac{1}{2}}=0; \tag{3.9}$$

- If $(\rho^-_{j+\frac{1}{2}},q^-_{j+\frac{1}{2}})\in\Omega_c$ and $(\rho^+_{j+\frac{1}{2}},q^+_{j+\frac{1}{2}})\in L_f$, we take

$$\begin{aligned} a^+_{j+\frac{1}{2}}&=\max\Big\{\lambda^c_2\big(\boldsymbol{U}^-_{j+\frac{1}{2}}\big),\lambda^f_2\big(\boldsymbol{U}^+_{j+\frac{1}{2}}\big),0\Big\}=\max\Big\{\lambda^c_2\big(\boldsymbol{U}^-_{j+\frac{1}{2}}\big),V_{\max},0\Big\}=V_{\max},\\ a^-_{j+\frac{1}{2}}&=\min\Big\{\lambda^c_1\big(\boldsymbol{U}^-_{j+\frac{1}{2}}\big),\lambda^f_1\big(\boldsymbol{U}^+_{j+\frac{1}{2}}\big),0\Big\}=\min\Big\{\lambda^c_1\big(\boldsymbol{U}^-_{j+\frac{1}{2}}\big),V_{\max},0\Big\}=\min\Big\{\lambda^c_1\big(\boldsymbol{U}^-_{j+\frac{1}{2}}\big),0\Big\}; \end{aligned} \tag{3.10}$$

- If $(\rho^-_{j+\frac{1}{2}},q^-_{j+\frac{1}{2}})\in L_f$ and $(\rho^+_{j+\frac{1}{2}},q^+_{j+\frac{1}{2}})\in\Omega_c$, we take

$$\begin{aligned} a^+_{j+\frac{1}{2}}&=\max\Big\{\lambda^f_2\big(\boldsymbol{U}^-_{j+\frac{1}{2}}\big),\lambda^c_2\big(\boldsymbol{U}^+_{j+\frac{1}{2}}\big),0\Big\}=\max\Big\{V_{\max},\lambda^c_2\big(\boldsymbol{U}^+_{j+\frac{1}{2}}\big),0\Big\}=V_{\max},\\ a^-_{j+\frac{1}{2}}&=\min\Big\{\lambda^f_1\big(\boldsymbol{U}^-_{j+\frac{1}{2}}\big),\lambda^c_1\big(\boldsymbol{U}^+_{j+\frac{1}{2}}\big),0\Big\}=\min\Big\{V_{\max},\lambda^c_1\big(\boldsymbol{U}^+_{j+\frac{1}{2}}\big),0\Big\}=\min\Big\{\lambda^c_1\big(\boldsymbol{U}^+_{j+\frac{1}{2}}\big),0\Big\}. \end{aligned} \tag{3.11}$$

Notice that in the computation of $a^{\pm}_{j+\frac{1}{2}}$ in Eqs. (3.10) and (3.11), we have used the fact that $\lambda^c_1\big(\boldsymbol{U}^{\pm}_{j+\frac{1}{2}}\big)\le\lambda^c_2\big(\boldsymbol{U}^{\pm}_{j+\frac{1}{2}}\big)\le V_{c+}\le V_{\max}$.

Finally, the term $\boldsymbol{Q}_{j+\frac{1}{2}}$ in Eq. (3.3) represents a "built-in" anti-diffusion and is given by [17]

$$\boldsymbol{Q}_{j+\frac{1}{2}}=\operatorname{minmod}\Big(\boldsymbol{U}^+_{j+\frac{1}{2}}-\boldsymbol{U}^*_{j+\frac{1}{2}},\boldsymbol{U}^*_{j+\frac{1}{2}}-\boldsymbol{U}^-_{j+\frac{1}{2}}\Big), \tag{3.12}$$

where

$$\boldsymbol{U}^*_{j+\frac{1}{2}}=\frac{a^+_{j+\frac{1}{2}}\boldsymbol{U}^+_{j+\frac{1}{2}}-a^-_{j+\frac{1}{2}}\boldsymbol{U}^-_{j+\frac{1}{2}}-\Big\{\boldsymbol{F}\big(\boldsymbol{U}^+_{j+\frac{1}{2}}\big)-\boldsymbol{F}\big(\boldsymbol{U}^-_{j+\frac{1}{2}}\big)\Big\}}{a^+_{j+\frac{1}{2}}-a^-_{j+\frac{1}{2}}}. \tag{3.13}$$

The ODE system Eqs. (3.2)–(3.3) has to be numerically integrated using an appropriate ODE solver. Upon completion of every time step (or every stage of a Runge-Kutta method), we project the obtained set of $(\bar\rho_j,\bar q_j)$ onto either L_f or Ω_c according to the procedure introduced in Appendix 3.1.

3.1. Projection onto L_f or Ω_c

Assume that we have obtained a set of data (either reconstructed point values or evolved cell averages) for ρ and q. If a certain pair $(\widetilde\rho,\widetilde q)$ is neither on L_f or in Ω_c, we have to project it onto either L_f or Ω_c according to the following four possible cases:

Case I: If $\widetilde\rho\le\rho^f_{\rm cr}$, which means that $\widetilde\rho$ corresponds to the free flow, we replace $\widetilde q$ with $q(\widetilde\rho)$ computed using Eq. (2.4);

Case II: If $\rho_{\rm cr}^f < \widetilde{\rho} < \rho_{\rm cr}^c$ and $\widetilde{q} > \dfrac{\widetilde{\rho}\rho_{\max}}{\rho_{\max}-\widetilde{\rho}}V_{c+}$, that is, the point $(\widetilde{\rho},\widetilde{q})$ is above the line L_3 (see Fig. 2.1), we shift this point vertically down to L_3 and replace $\widetilde{q}$ with $\dfrac{\widetilde{\rho}\rho_{\max}}{\rho_{\max}-\widetilde{\rho}}V_{c+}$;

Case III: If $\rho_{\rm cr}^c < \widetilde{\rho}$ and $\widetilde{q} > q^* + \dfrac{q^+-q^*}{\rho_{\max}}\widetilde{\rho}$, that is, the point $(\widetilde{\rho},\widetilde{q})$ is above the line L_1 (see Fig. 2.1), we shift this point vertically down to L_1 and replace $\widetilde{q}$ with $q^* + \dfrac{q^+-q^*}{\rho_{\max}}\widetilde{\rho}$;

Case IV: If $\rho_{\rm cr}^f < \widetilde{\rho}$ and $\widetilde{q} < q^* + \dfrac{q^--q^*}{\rho_{\max}}\widetilde{\rho}$, that is, the point $(\widetilde{\rho},\widetilde{q})$ is below the line L_2 (see Fig. 2.1), we shift this point vertically up to L_2 and replace $\widetilde{q}$ with $q^* + \dfrac{q^--q^*}{\rho_{\max}}\widetilde{\rho}$.

Note that in all of these four cases, we modify q only without changing ρ so that vehicles are not getting artificially added to or removed from the road.

4. Numerical examples

In this section, we evaluate the performance of the proposed numerical scheme using extensive numerical tests. To this end, we use the three-stage third-order strong stability preserving (SSP) Runge-Kutta method (see, e.g., [26,27]) in order to numerically solve the ODE system Eqs. (3.2) and (3.3) using the CFL number 0.4, which is selected based on our initial investigation findings.

For clarity and better organization, we categorize our investigation scenarios into two main types based on the similarities in initial and boundary conditions. The first category includes Riemann problems with simple free boundary conditions (Examples 1 and 2), while the second category consists of more realistic, traffic-oriented cases (Examples 3 and 4), where complex Dirichlet boundary conditions are imposed at the downstream boundary to simulate traffic situations that induce backward-propagating waves. In all of our examples, we employ the parameters listed in Table 4.1, which include both the phase-transition model settings and the physicality constraints for the congested domain. These parameters are chosen to reflect empirical traffic conditions: the free-flow speed is set to 30 m/s, consistent with typical freeway speed limits; the maximum density ranges from 110 to 170 veh/km based on average vehicle size and spacing; and the critical density is defined as 15–30 % of the maximum density. The time gap and the bounds q^+ and q^- are also selected from typical empirical ranges, as discussed in [1,8].

Example 1. In the first example, we consider several Riemann initial data of the form

$$\boldsymbol{U}(x,0) = \begin{cases} \boldsymbol{U}_L & \text{if } x < x_0, \\ \boldsymbol{U}_R & \text{otherwise,} \end{cases} \qquad x_0 = 40000, \tag{4.1}$$

prescribed in the computational domain $[0, 800000]$ subject to the free boundary conditions. This setting corresponds to a Riemann problem on a long road with open boundaries.

Table 4.2 presents twelve comprehensive test cases used in our first example, along with the essential information about traffic states on either side of the initial discontinuity. All of these test cases are numerically challenging and can give rise to complex waves, comprising of multiple wave types such as shock waves, contact discontinuities, and rarefaction waves due to involving transitions between the free-flow and congested phases.

In Tests 1–5, free-flow traffic upstream of the initial discontinuity encounters congested traffic downstream. In all of these test cases, vehicles in the upstream will have to decelerate in order to adapt to the traffic conditions downstream, and the solution would involve shock waves. While these test cases are quite comparable in terms of traffic speed on either side of the initial discontinuity, there are significant differences in the sign and magnitude of $q - q^*$ on the right-hand side (RHS), which result in different driving behaviors and are expected to manifest in the corresponding traffic waves. In general, the farther the quantity $q - q^*$ is from zero, the greater the deviation of the drivers' *average time gap*, $1/q$, from the equilibrium time gap, $1/q^*$ (the time gap corresponding to the equilibrium speed-density relationship in Eq. (2.3) with $q = q^*$).

Therefore, in scenarios where $q - q^* > 0$ on the RHS (Tests 1–3), drivers' average time gap on this side of the discontinuity is already smaller than the equilibrium time gap, which implies more aggressive driving behavior and a tendency toward denser traffic. In these cases, an intermediate state is expected to form, connecting the upstream free-flow to the congested downstream, as q on the RHS is larger than equilibrium. In contrast, in scenarios where $q - q^* < 0$ on the RHS (Tests 4 and 5), drivers' average time gap is larger than the equilibrium time gap, and an intermediate state is not expected to arise, as the q on the RHS of the discontinuity is already smaller than the equilibrium.

Table 4.1
Parameters of the phase-transition model adopted for numerical tests.

Parameter	$V_{\max}$	V_{c+}	$\rho_{\max}$	q^*	$\rho_{\rm cr}^f$	q^+	q^-
Value	30	24	0.16	0.6	0.02	0.93186	0.18856

Table 4.2
Initial conditions for Tests 1–12.

Test	Left-side				Right-side			
	Phase	ρ_L	V_L	$q_L - q^*$	Phase	ρ_R	V_R	$q_R - q^*$
1	Free	0.011	30	-0.2456	Congested	0.0825	4.5113	0.1684
2	Free	0.011	30	-0.2456	Congested	0.0775	4.5945	0.0906
3	Free	0.0075	30	-0.3639	Congested	0.0675	5.338	0.02325
4	Free	0.001	30	-0.5698	Congested	0.0625	4.73	-0.1149
5	Free	0.001	30	-0.5698	Congested	0.0875	2.9945	-0.02175
6	Congested	0.128	0.42321	-0.3291	Congested	0.0375	13.838	0.07778
7	Congested	0.0375	13.838	0.07778	Congested	0.128	0.42321	-0.3291
8	Congested	0.0825	4.5113	0.1684	Free	0.011	30	-0.2456
9	Congested	0.0775	4.5945	0.0906	Free	0.011	30	-0.2456
10	Congested	0.0675	5.338	0.02324	Free	0.0075	30	-0.3639
11	Congested	0.0625	4.73	-0.1149	Free	0.001	30	-0.5698
12	Congested	0.0875	2.9945	-0.02175	Free	0.001	30	-0.5698

Tests 6 and 7 represent scenarios in which there is no phase transition, as the traffic states on both sides of the initial discontinuity are in a congested phase. From a computational and numerical standpoint, these test cases are less challenging. However, they are included for their physical significance, namely, to examine the model's solution structure for Riemann problems where one state's time gap is close to the equilibrium, while the other exhibits a deviation from this equilibrium.

In Tests 8–12, traffic state in the upstream of the initial discontinuity is congested, whereas free-flow traffic exists in the downstream. As a result, vehicles in the upstream will go through acceleration speed adaptation manoeuvres in order to adapt to the traffic condition in the downstream. These cases encompass a variety of transitions between traffic phases, characterized by the fluctuation of the quantity $q - q^*$ across a spectrum of values, from negative to positive. This variation indicates diverse scenarios where drivers' average preferred time gap deviates from the equilibrium time gap, and are considered in the numerical tests for two aspects: (a) to evaluate and demonstrate the performance of the proposed scheme under such complex phase-transitions and (b) to shed light on the phase-transition model's solution structures for such initial discontinuities and provide physical interpretations.

We compute the solutions until the final time $T_{\text{final}} = 900$ by the proposed CU scheme on the computational domain $[0, 80000]$ on the uniform mesh with $\Delta x = 200$ subject to the free boundary conditions. We present the obtained results in Figs. 4.1–4.3 together with the reference solution computed on a much finer mesh with $\Delta x = 5$. As one can see, the developed CU scheme can capture the solution structures of these Riemann problems in an non-oscillatory manner and the achieved resolution is high.

Example 2. In the second example, we take the computational domain $[0, L]$ with $L = 10000$ and consider the following initial conditions:

$$\rho(x,0) = \begin{cases} 0.01 & \text{if } x \le \frac{L}{3}, \\ 0.03 & \text{if } \frac{L}{3} < x \le \frac{2L}{3}, \\ 0.04 & \text{otherwise}, \end{cases} \quad V(x,0) = \begin{cases} 30 & \text{if } x \le \frac{L}{3}, \\ 17.729 & \text{if } \frac{L}{3} < x \le \frac{2L}{3}, \\ 11.812 & \text{otherwise}, \end{cases} \tag{4.2}$$

shown in Fig. 4.4 (top row). The corresponding values of the quantity $q - q^*$ are then

$$q(x,0) - q^* = \begin{cases} -0.2800 & \text{if } x \le \frac{L}{3}, \\ 0.0546 & \text{if } \frac{L}{3} < x \le \frac{2L}{3}, \\ 0.0300 & \text{otherwise}. \end{cases} \tag{4.3}$$

This test case is numerically challenging and physically complex due to the formation and propagation of multiple interacting compound waves traveling in different directions. Specifically, the traffic dynamics vary across the domain: the region $x \le \frac{L}{3}$ exhibits free-flowing traffic, which progresses to moderate congestion in the range $\frac{L}{3} < x \le \frac{2L}{3}$, and escalates to dense traffic when $x > \frac{2L}{3}$. The initial conditions feature two discontinuities in speed and density profiles. As $q(x,0) - q^* \neq 0$ for all x, compound waves are anticipated at the interfaces of these discontinuities.

We compute the numerical results using the proposed CU scheme until the final time $T_{\text{final}} = 250$ on a uniform mesh with $\Delta x = 25$ subject to the following Dirichlet boundary conditions imposed at the left end of the computational domain $x = 0$:

$$\rho(0,t) = 0.01, \quad q(0,t) = \frac{\rho(0,t) V_{\max}}{1 - \rho(0,t)/\rho_{\max}}, \tag{4.4}$$

and free boundary conditions at the right end of the computational domain.

The computed ρ and V at times $t = 50$, 200, and 250 are presented in Fig. 4.4 together with a reference solution calculated on a finer mesh with $\Delta x = \frac{5}{4}$. The comparison underscores the scheme's robust capability to capture solution structures

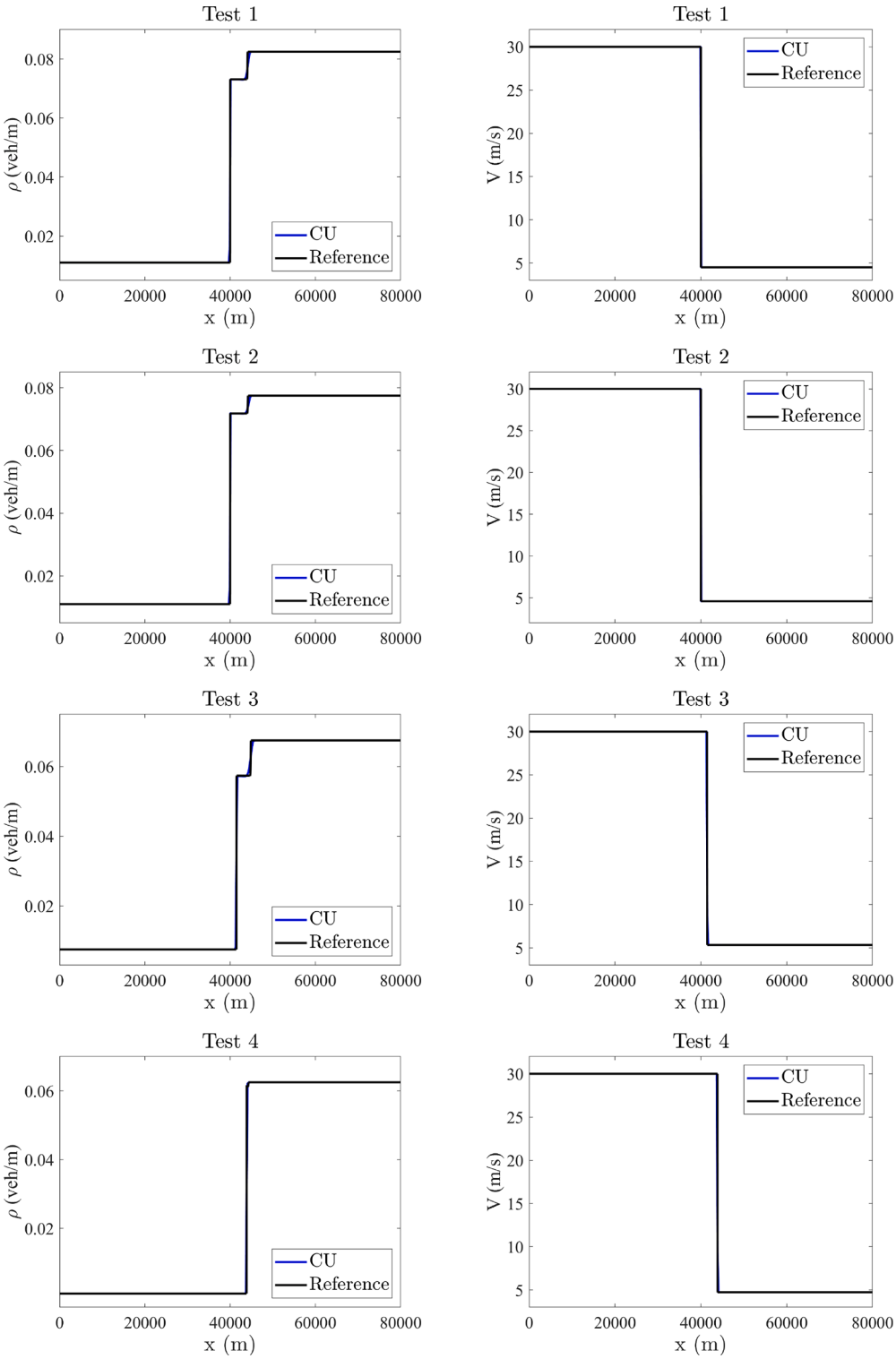

Fig. 4.1. Example 1, Tests 1–4: ρ (left column) and V (right column) at time $T_{\text{final}} = 900$.

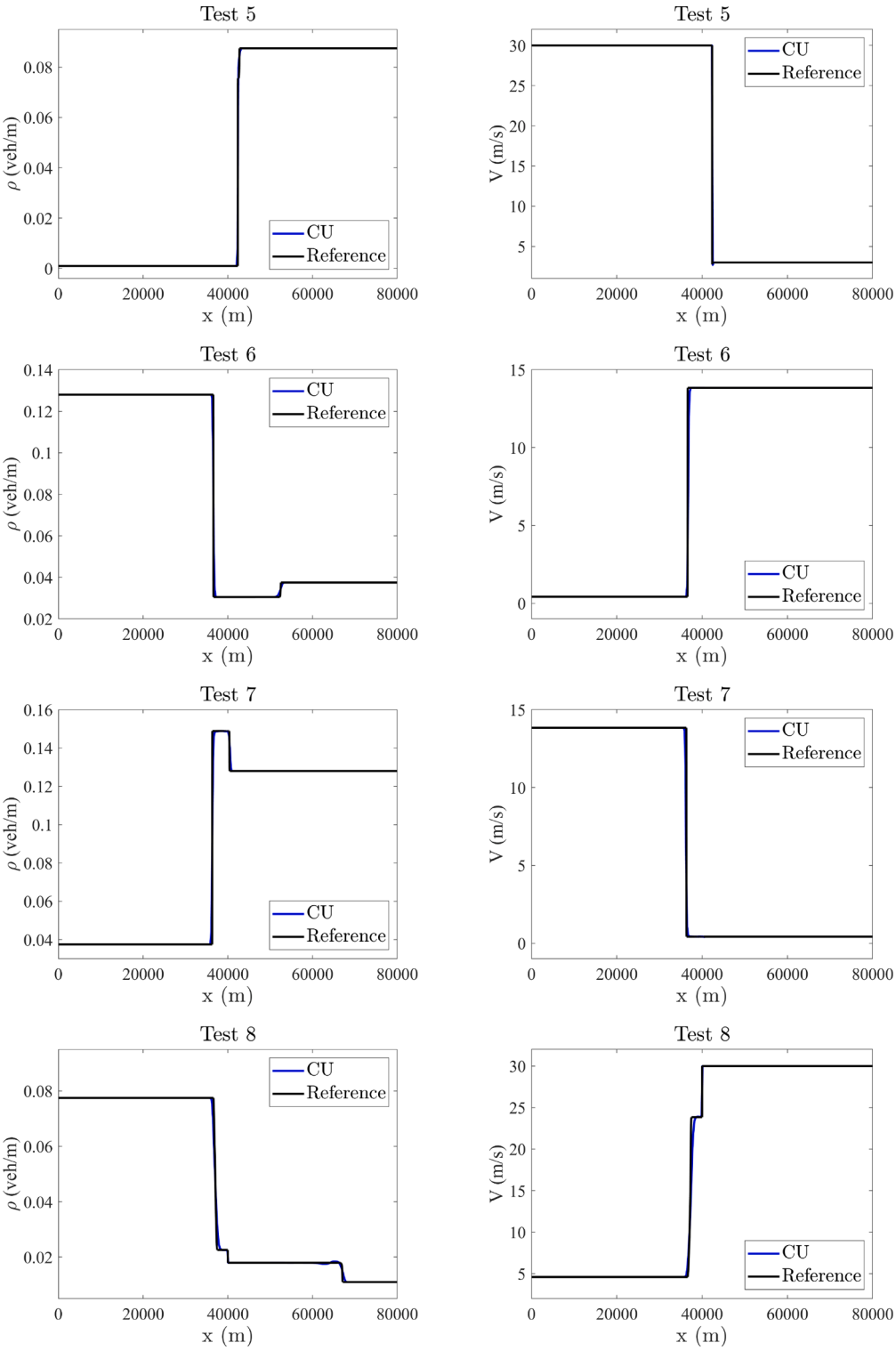

Fig. 4.2. Example 1, Tests 5–8: ρ (left column) and V (right column) at time $T_{\text{final}} = 900$.

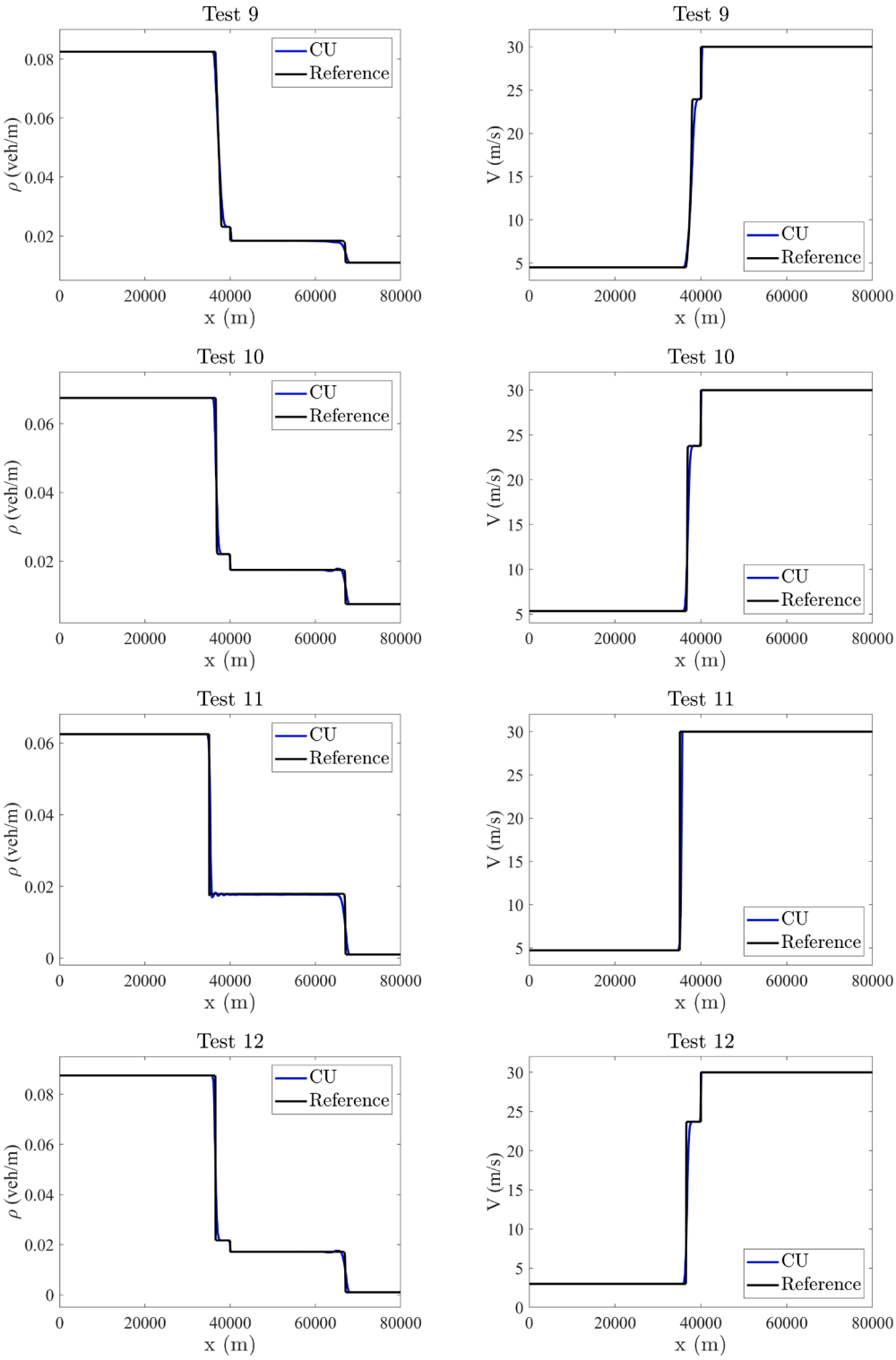

Fig. 4.3. Example 1, Tests 9–12: ρ (left column) and V (right column) at time $T_{\text{final}} = 900$.

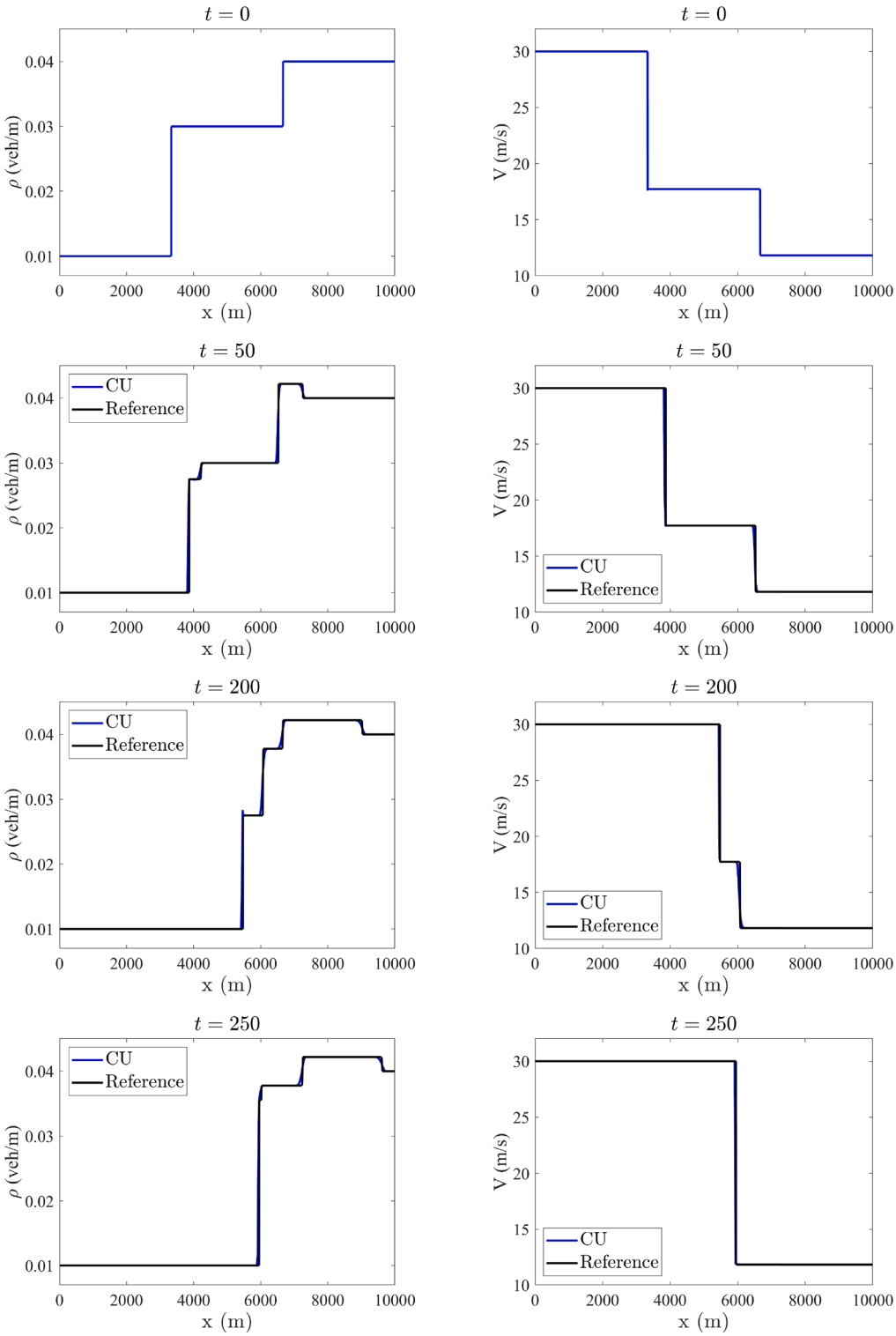

Fig. 4.4. Example 2: ρ (left column) and V (right column) at times $t = 0$ (top row), $t = 50$ (second row), $t = 200$ (third row), and $t = 250$ (bottom row).

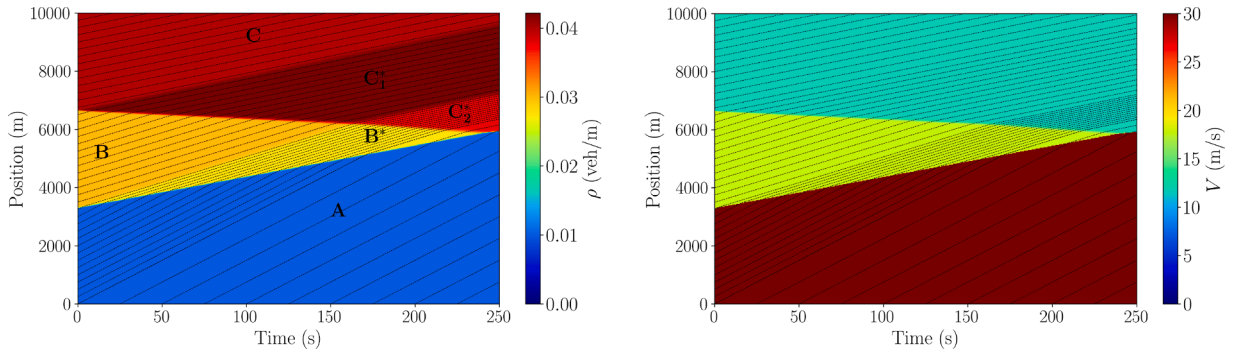

Fig. 4.5. Example 2: Spatio-temporal evolution of ρ (left) and V (right) for $t \in [0, 250]$.

arising from interacting waves. It maintains sharpness near contact discontinuities and shock waves, while ensuring non-oscillatory behavior.

Let us now examine the spatio-temporal evolution of traffic density and speed. In Fig. 4.5, we present time-space diagrams for both variables, with representative vehicle trajectories superimposed—both from vehicles placed every 100 m along the road at the initial time and those released every 50 s from the upstream boundary at $x = 0$. These vehicle trajectories can be viewed as phantom moving observers traveling with the local average traffic speed and adapting their dynamics to prevailing flow conditions. The spatio-temporal analysis of traffic density indicates that it can be divided into six distinct regions (each characterized by a constant density), which are labeled as A, B, B*, C, C_1^*, and C_2^* in Fig. 4.5 (left). Note that the traffic speed remains invariant across Regions B, B*, and also across C, C_1^*, and C_2^*. We shall elaborate on the waves arising at the interface between these regions.

In order to interpret the results physically, we consider the region defined by $\frac{L}{3} < x < \frac{2L}{3}$ in the initial conditions as the reference point, referred to as Region B in Fig. 4.5 (left). In Region B, $q(x, 0) - q^* > 0$, suggesting that the inter-vehicular spacing is initially smaller than the equilibrium spacing, and consequently, the traffic density is higher than would be expected with initial $q - q^* = 0$. At time $t = 0$, Region B is flanked upstream by a free-flow region ($x < \frac{L}{3}$, Region A) with very low density, and downstream by a denser traffic condition ($x > \frac{2L}{3}$, Region C). As a result, compound waves form at both ends of Region B. To facilitate discussion on these waves, it is important to clarify that henceforth, the endpoints of each region in the spatial domain will be referred to as the right-end (downstream) and left-end (upstream), respectively.

At the left end of Region B, an intermediate state (Region B*) emerges and separates Regions A and B with a shockwave at the left end of Region B* (corresponding to λ_1 and traveling forward due to the lower density in Region A) and a contact discontinuity at the right end (corresponding to λ_2). In Region B*, the traffic speed matches that of Region B, while the density is intermediate between that of Regions A and B. Since the speed of the shockwave is smaller in magnitude compared to the speed of the contact discontinuity at the interface between Regions B* and B, Region B* expands spatially over time. This expansion continues until the contact discontinuity ceases to exists around $x = 6200$ m and $t = 160$ s.

At the right end of Region B, another intermediate state, Region C_1^*, emerges, separating Regions B and C. Region C_1^* is characterized by a shockwave at the left end (corresponding to λ_1 and traveling backward due to congestion) and a contact discontinuity at the right end (corresponding to λ_2). Within Region C_1^*, the traffic speed is consistent with that of Region C, while the density is intermediate between those in Regions B and C.

At a specific point in time and space (specifically, around $x = 6200$ m and $t = 160$ s), the shockwave traveling backward at the left end of Region C_1^* meets the contact discontinuity traveling forward at the right end of Region B*. This interaction leads to the formation of Region C_2^*, which is confined by a shockwave traveling backward and a contact discontinuity traveling forward.

Example 3. In this example, we take the computational domain $[0, L]$ with $L = 10000$ and consider the following initial conditions:

$$\rho(x,0) = \begin{cases} 0.01 & \text{if } x \le \frac{L}{3}, \\ 0.03 & \text{if } \frac{L}{3} < x \le \frac{2L}{3}, \\ 0.05 & \text{otherwise}, \end{cases} \quad V(x,0) = \begin{cases} 30 & \text{if } x \le \frac{L}{3}, \\ 17.729 & \text{if } \frac{L}{3} < x \le \frac{2L}{3}, \\ 7.941 & \text{otherwise}, \end{cases} \tag{4.5}$$

presented in Fig. 4.6 (top row). The corresponding values of the quantity $q - q^*$ are then

$$q(x,0) - q^* = \begin{cases} -0.2800 & \text{if } x \le \frac{L}{3}, \\ 0.0546 & \text{if } \frac{L}{3} < x \le \frac{2L}{3}, \\ -0.0225 & \text{otherwise}. \end{cases} \tag{4.6}$$

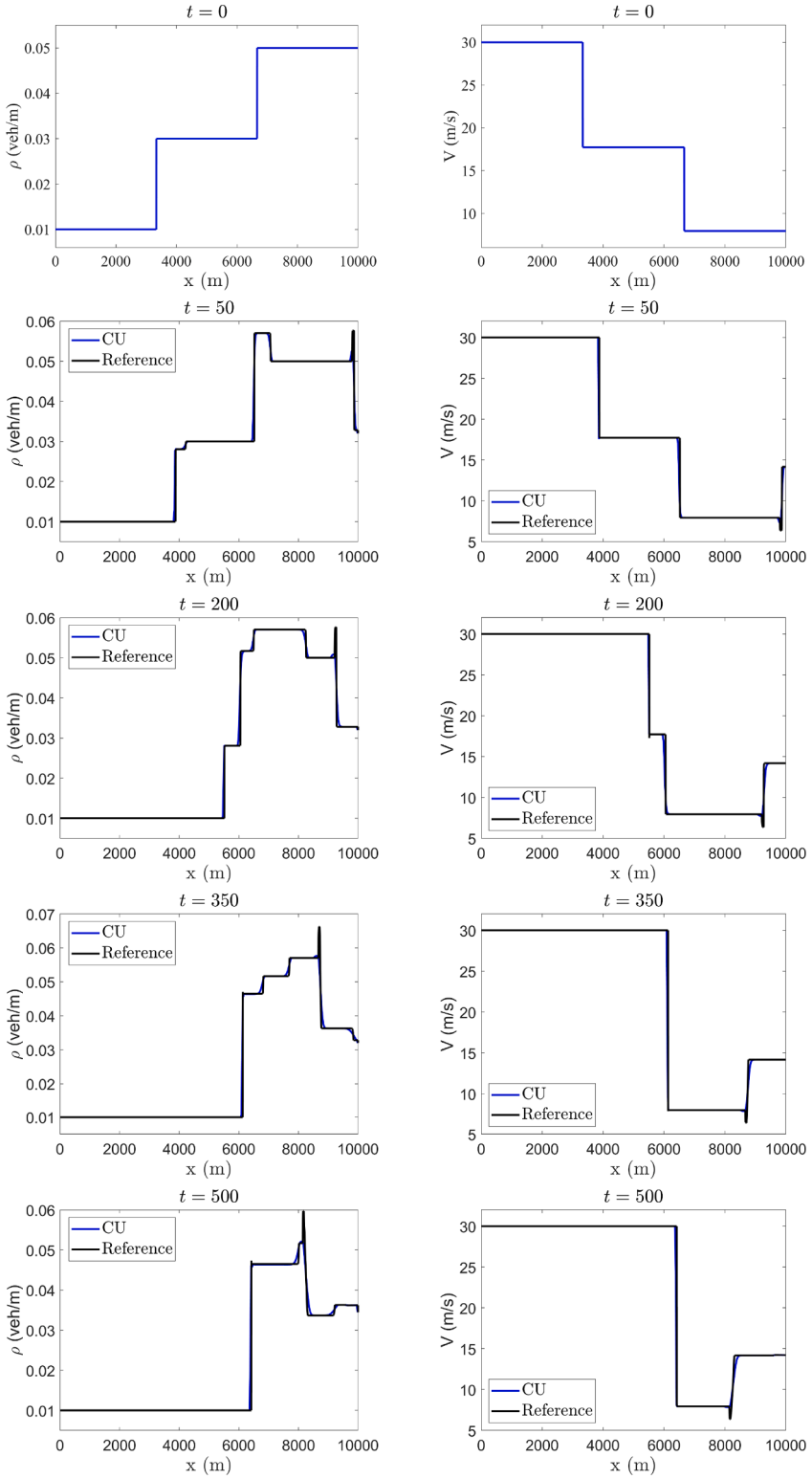

Fig. 4.6. Example 3: ρ (left column) and V (right column) at times $t = 0$ (top row), $t = 50$ (second row), $t = 200$ (third row), $t = 350$ (fourth row), and $t = 500$ (bottom row).

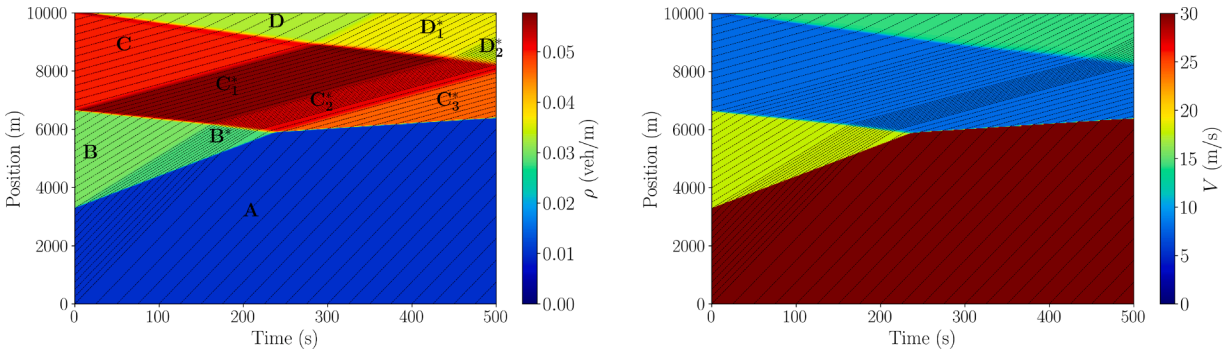

Fig. 4.7. Example 3: Spatio-temporal evolution of ρ (left) and V (right) for $t \in [0, 500]$.

In this example, the free boundary conditions are imposed at the left end of the computational domain, whereas at the right end of the computational domain, we impose the following Dirichlet boundary conditions:

$$\rho(L,t) = \begin{cases} 0.05 + 0.3\left[\cosh^{-2}\left(\dfrac{t-\frac{T_0}{2}}{W}\right) - \dfrac{1}{4}\cosh^{-2}\left(\dfrac{t-T_1-\frac{T_0}{2}}{W}\right)\right], & t \le \dfrac{2}{3}T_{\text{final}}, \\ 0.03 + 0.2\left[\cosh^{-2}\left(\dfrac{t-T_0}{W}\right) - \dfrac{1}{4}\cosh^{-2}\left(\dfrac{t-T_1-T_0}{W}\right)\right], & \text{otherwise}, \end{cases}$$

$$q(L,t) = \begin{cases} \dfrac{21}{4}\rho_{\max}\left(1 + (a-1)\dfrac{\rho(L,t)}{\rho_{\max}} - \left[\left(a\dfrac{\rho(L,t)}{\rho_{\max}}\right)^{20} + \left(1 - \dfrac{\rho(L,t)}{\rho_{\max}}\right)^{20}\right]^{\frac{1}{20}}\right), & \rho(L,t) > \rho^f_{\text{cr}} \\ \rho(L,t)V_{\max}\left(1 - \dfrac{\rho(L,t)}{\rho_{\max}}\right)^{-1}, & \text{otherwise}. \end{cases} \tag{4.7}$$

Here, $W = 201.25$, $T_0 = 1500$, $T_1 = 3000$, $T_{\text{final}} = 250$, and $a = \frac{30}{7}$.

While qualitatively similar to previous examples, this case is more complex due to a time-varying downstream boundary condition, leading to the formation of additional wave types and regions. Another key difference is at the interface between the two congestion regions (initially located at $x > \frac{L}{3}$), where upstream vehicles have smaller inter-vehicular spacing than at equilibrium ($q - q^* > 0$), and downstream vehicles have larger spacing ($q - q^* < 0$). This results in multiple intermediate states and interacting waves, which are challenging to capture in a non-oscillatory manner; see [28].

We compute the numerical results using the proposed CU scheme until $t = T_{\text{final}}$ on a uniform mesh with $\Delta x = 25$. The computed values of ρ and V at $t = 50$, 200, 350, and 500 are shown in Fig. 4.6 together with a reference solution computed on a finer mesh with $\Delta x = \frac{5}{4}$. As one can see, the scheme accurately captures solution structures from interacting waves, while staying sharp near shock waves and contact discontinuities and remaining non-oscillatory around intermediate states.

To interpret the numerical results physically, we examine the spatio-temporal evolution of traffic density and speed in Fig. 4.7, where time-space diagrams are shown with superimposed vehicle trajectories similar to those in Fig. 4.5. The comparison between speed and density graphs reveals that the solution domain can be divided into four regions where speed is constant; see Fig. 4.7 (right). The density in these regions is, however, not constant except for the free-flow Region A. The other regions with constant speed can be further divided into subregions with constant density, labeled as B, B^*_1, C, C^*_1, C^*_2, C^*_3, D, D^*_1, and D^*_2.

Let us begin a discussion on the physical interactions with the wave types arising at the initial discontinuities between the three main Regions A, B, and C in the initial condition. The Riemann solution at the left end of Region B involves the formation and expansion of Region B* between Regions A and B. Region B* is characterized by a shockwave moving upstream (backward) and a contact discontinuity traveling forward (downstream) at a faster rate than the shockwave. Meanwhile, at $x = 2L/3$ and $t = 0$, one observes the formation of a shockwave traveling backward, causing Region B to shrink, as well as a contact discontinuity traveling forward, which leads to the formation of a high-density intermediate state (Region C^*_1) between Regions B and C.

At approximately $x = 6200$ m and $t = 160$ s, the contact discontinuity at the left end of Region B catches up with the shockwave traveling backward at the right end of Region B, leading to the formation of Region C^*_2 and the clearance of Region B. Region C^*_2 spans backward until around $x = 5900$ m and $t = 220$ s, when Region B* is cleared as the shockwave at the left end of Region B* meets the contact discontinuity at the right end of Region B*. This interaction leads to the formation of Region C^*_3, which arises as an intermediate state between another shockwave traveling upstream and a contact discontinuity traveling downstream.

Finally, at $x = L$ and $t = 0$, a shockwave arises traveling backward as the congested state in Region C discharges from the downstream, which leads to the formation of another intermediate state between Region C and the downstream boundary (Region D).

At approximately $x = 9000$ m and $t = 280$ s, the shockwave traveling forward at the upper end of Region D meets the contact discontinuity traveling forward at the lower end of Region C. This interaction forms region D*, characterized by a compound wave: a contact discontinuity moving forward at the left end of region D^*_1 and a shockwave moving upstream at a slightly slower rate at the lower end of region D^*_1.

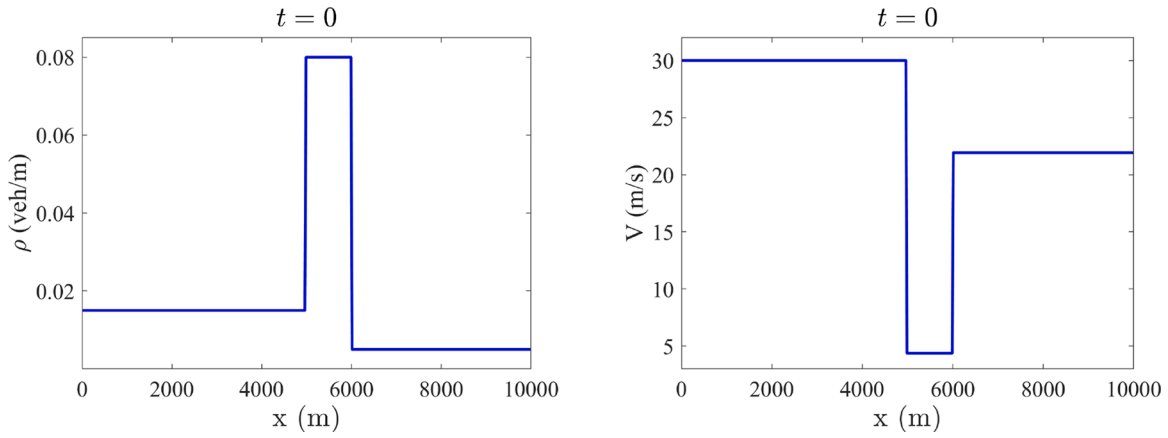

Fig. 4.8. Example 4: Initial conditions for ρ (left) and V (right).

Region D_1^* persists until approximately $x = 8500\,\text{m}$ and $t = 440\,\text{s}$, when the shockwave at the lower end of region D_1^* meets the contact discontinuity at the right end of region C_1^*, forming region D_2^*. This leads to another compound wave with a shockwave traveling upstream at the lower end of region D_2^* and a contact discontinuity in region D_2^*.

Example 4. In our final example, we aim to reconstruct a tangible real-world scenario using initial and boundary conditions that are widely observable in real-world traffic. We take the computational domain $[0, L]$ with $L = 10000$ and assume the following initial conditions:

$$\rho(x,0) = \begin{cases} 0.015 & \text{if } x \le \frac{L}{2}, \\ 0.08 & \text{if } \frac{L}{2} < x \le \frac{3L}{5}, \\ 0.025 & \text{otherwise}, \end{cases} \quad V(x,0) = \begin{cases} 30 & \text{if } x \le \frac{L}{2}, \\ 4.375 & \text{if } \frac{L}{2} < x \le \frac{3L}{5}, \\ 21.94 & \text{otherwise}, \end{cases} \tag{4.8}$$

presented in Fig. 4.8. The corresponding values of the quantity $q - q^*$ are then

$$q(x,0) - q^* = \begin{cases} -0.1034 & \text{if } x \le \frac{L}{2}, \\ 0.1 & \text{if } \frac{L}{2} < x \le \frac{3L}{5}, \\ 0.0501 & \text{otherwise}. \end{cases} \tag{4.9}$$

The initial conditions in this scenario depict a strong bottleneck with highly congested traffic, represented as an initial queue in the middle section of a freeway. At the left end of the computational domain, we impose a free upstream boundary condition, while at the right end, we assume the downstream boundary conditions are time-dependent and periodic to reflect a stop-and-go traffic condition further downstream. Note that in traffic flow, drivers mainly respond to conditions ahead, and the majority of traffic waves propagate backward. Therefore, if the situation further downstream is congested, the outflow cannot exit. This example is practically relevant, as such stop-and-go patterns are widely observable in real-world traffic. The downstream boundary condition is mathematically expressed as

$$\begin{aligned} \rho(L,t) &= \begin{cases} 0.03 + 0.03\left[\cosh^{-2}\left(\frac{t - T_0}{W}\right) - 2.05\cosh^{-2}\left(\frac{t - T_1 - T_0}{W}\right)\right], & t \le 1000, \\ 0.03, & 1000 < t < 1200, \\ 0.01, & \text{otherwise}, \end{cases} \\ q(L,t) &= \begin{cases} \frac{21}{4}\rho_{\max}\left(1 + (a-1)\frac{\rho(L,t)}{\rho_{\max}} - \left[\left(a\frac{\rho(L,t)}{\rho_{\max}}\right)^{20} + \left(1 - \frac{\rho(L,t)}{\rho_{\max}}\right)^{20}\right]^{\frac{1}{20}}\right), & t < 1200, \\ \rho(L,t)V_{\max}\left(1 - \frac{\rho(L,t)}{\rho_{\max}}\right)^{-1}, & \text{otherwise}, \end{cases} \end{aligned} \tag{4.10}$$

which are illustrated in Fig. 4.9. Here, $W = 10.25$, $T_0 = \lfloor \frac{t}{100} \rfloor + 50$, $T_1 = 3000$, and $a = \frac{30}{7}$.

This scenario is common in real-world traffic. On a homogeneous road without on- or off-ramps, we assume the initial queue in the middle can represent traffic conditions after a crash that occurred at $x = 3L/5$ before the simulation, with the crash scene persisting for a while. This results in very slow queue discharge and light traffic conditions downstream in the area $x > 3L/5$ until the crash scene is cleared at $t = 0$. Additionally, the downstream boundary condition involves stop-and-go traffic up until $t = 1000\,\text{s}$, then transitions to a mildly congested state between $t = 1000\,\text{s}$ and $t = 1200\,\text{s}$, followed by free-flow traffic again for $t > 1200\,\text{s}$. Stop-and-go traffic at the downstream boundary is assumed to result from highly periodic incoming flow through a hypothetical on-ramp further

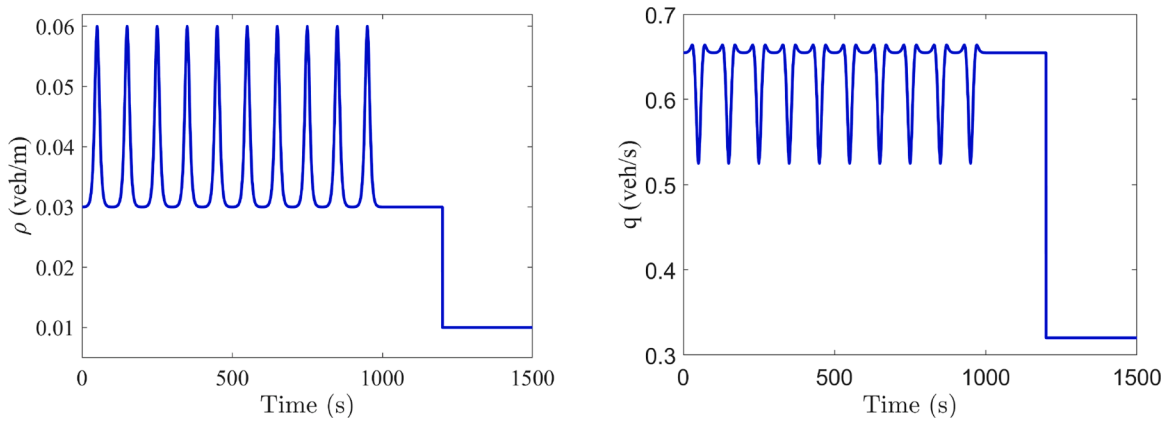

Fig. 4.9. Example 4: Boundary conditions for ρ and q at the right end of the computational domain.

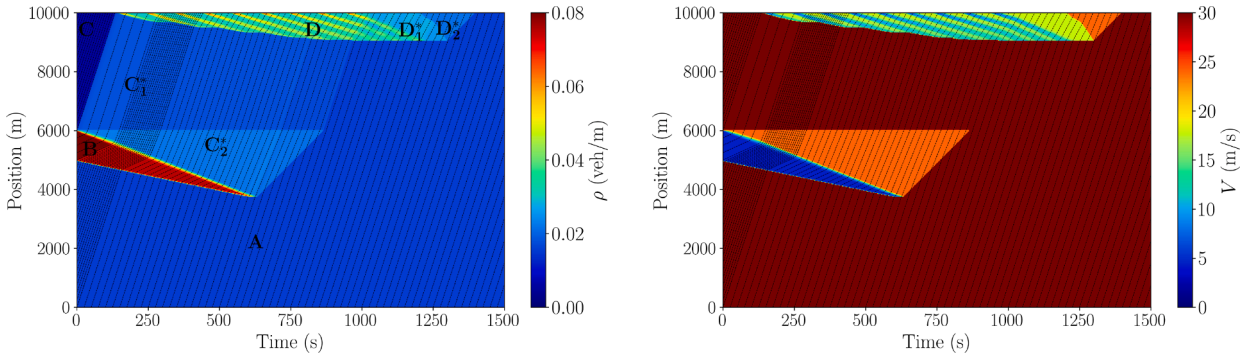

Fig. 4.10. Example 4: Spatio-temporal evolution of ρ (left) and V (right) for $t \in [0, 1500]$.

downstream in the computational domain. Our aim is to investigate the spatio-temporal evolution of traffic flow in a complex scenario involving multiple interacting bottlenecks. This test case provides a good basis for examining these interactions while demonstrating the performance of the proposed CU scheme and highlighting the physical implications of the results.

We compute the numerical results until the final time $T_{\text{final}} = 1500$ on a uniform mesh with $\Delta x = 25$. To stay focused, we present only the spatio-temporal evolution of density and speed in Fig. 4.10, which again shows that the proposed scheme can capture the overall structures of the numerical solution in a non-oscillatory manner.

To interpret the numerical results physically, we examine the spatio-temporal evolution of traffic density and speed. In Fig. 4.10, time-space diagrams are shown with superimposed vehicle trajectories similar to those in Figs. 4.5 and 4.7. We consider several regions (A, B, C_1^*, C_2^*, D, D_1^*, and D_2^*) in the density panel, which mark key phases of traffic evolution.

First, Region A corresponds to free-flow traffic entering from the upstream boundary. Second, we focus on the initial queue, highlighted as Region B, which involves a strong bottleneck. Region B is characterized by two backward-traveling shocks at its upper and lower ends. The shockwave at the lower end arises as free-flowing traffic encounters highly congested traffic, whereas the shockwave at the upper end arises as vehicles leave the congestion region. Note that the upper-end shock travels backward faster as vehicles leaving Region B adjust their speed to the maximum in the congested region ($V_{c+} = 24\,\text{m/s}$), and, as a result, at around $x = 3800\,\text{m}$ and $t = 600\,\text{s}$, the shockwaves meet, leading to the dissolution of Region B.

The upper end of Region B neighbors three regions with varying characteristics, as compound waves arise and interact at the interface between the initial queue and free-flow traffic. First, Region C is characterized by a contact discontinuity at its right end. In this region, vehicles maintain their free-flow initial condition. Due to the low traffic density, vehicles in Region C do not create backward-propagating waves when reaching $x = L$, where slow-moving stop-and-go traffic occurs.

Next, Region C_2^* remains congested, with vehicles adapting their speed to the maximum in the congestion domain Ω_c ($V_{c+} = 24\,\text{m/s}$). Region C_2^* is characterized by intermediate congestion, confined by three shocks at its upper, lower, and right ends. The shock at the lower end arises as vehicles leaving the highly congested bottleneck in Region B adjust their speed to the maximum in the congestion domain. The shock at the right end forms as vehicles from the free-flow Region A enter and pass through C_2^*. The shock at the upper end occurs during the transition from intermediate congestion to the free-flow domain, and as the traffic states neighboring in the either side of the shock, are in a relatively comparable range.

Finally, in Region C_1^*, free-flow traffic with a density close to ρ_{cr}^f persists. Region C_1^* is confined by a shock from the lower end, contact discontinuities at the left and right ends, and a backward-traveling shock wave with varying speed at the upper end, which

is the interface between Regions C_1^* and D. This shock wave arises due to the high traffic flow in Region C_1^*, and upon meeting the congested condition at the downstream boundary (see Fig. 4.9), it leads to the formation and backward propagation of the oscillatory Region D. We note that the interface between Regions C_1^* and D has a varying shock speed in the time-space diagram as the tiny cluster-like waves inside Region D also disperse and propagates forward. Region D continues to propagate backward until shortly after Region C_1^* is cleared (roughly at $x = 9300\,\text{m}$ and around $t = 950\,\text{s}$), at which point the last vehicles leaving Region C_2^* reach Region D. From this point onward, Region A with low density meets Region D from behind, causing the interface between the two regions to become a stationary shock. This stationary shock continues to remain as the downstream boundary condition (at $x = L$) is replaced with a steady congested state during $1000\,\text{s} < t < 1200\,\text{s}$. As the downstream boundary condition (at $x = L$) becomes free again for $t \geq 1200\,\text{s}$, a new Region D_2^* forms as vehicles in Region D_1^* leave the congested state. A shock wave arises at the interface between Regions D_1^* and D_2^*, traveling backward until it meets the free-flow Region A at approximately $x = 8300\,\text{m}$ and $t = 1650\,\text{s}$. From this point, a forward-traveling shock wave arises, causing the dissolution of Region D_2^* as vehicles adapt their dynamics to those in Region A.

5. Conclusions

Phase-transition hyperbolic traffic flow models meet most requirements for non-equilibrium traffic flow models, such as maintaining the anisotropy property, maintaining consistency with the inverse correlation between driver speed and intervehicular spacing, satisfying zero speed at maximum density, and distinctly representing dynamics in free-flow and congested phases. Phase-transition models incorporate “time-gap”, a key element of automated vehicle control logic, as a conserved variable in their equations of state, giving them significant potential for future applications in the era of connected and automated vehicles.

Despite their significant potential, phase-transition models have been largely overlooked in traffic flow theory, particularly in numerical simulations and analysis. This gap is due to the mathematical complexity of these models, such as their discontinuous solution domains and fluxes, which make them challenging to simulate numerically.

This paper presents the development of a second-order semi-discrete finite-volume central-upwind scheme for the phase-transition traffic flow model. The developed scheme has been applied to several challenging numerical examples, demonstrating its ability to capture numerical solution structures sharply and without oscillations. Using this method, the phase-transition model’s performance was studied in various real-world traffic scenarios, in which multiple traffic phases interact, leading to interacting bottlenecks and complex solution structures. Such investigations were previously infeasible, but the proposed numerical method now facilitates the implementation of the model in complex real-world traffic scenarios.

There are several future directions for this work. First, future studies can utilize the proposed numerical scheme in conjunction with real-world traffic data to apply optimization-based parameter estimation of the phase-transition model and investigate the performance of the calibrated model against real-world traffic phenomena. Second, the proposed numerical scheme solves traffic flow on homogeneous roads without junctions or interchanges. Future work can extend this freeway-level solver by incorporating boundary coupling conditions at junctions to implement the phase-transition model on complex networks with multiple interacting bottlenecks. Such approaches are crucial for model-predictive optimization of traffic networks. These topics are currently being investigated in ongoing work by the authors.

CRediT authorship contribution statement

Shaoshuai Chu: Writing – review & editing, Writing – original draft, Visualization, Validation, Software, Methodology, Investigation, Conceptualization; **Alexander Kurganov:** Writing – review & editing, Writing – original draft, Validation, Supervision, Resources, Project administration, Methodology, Investigation, Funding acquisition, Conceptualization; **Saeed Mohammadian:** Writing – review & editing, Writing – original draft, Visualization, Validation, Methodology, Investigation, Data curation, Conceptualization; **Zuduo Zheng:** Writing – review & editing, Supervision, Resources, Conceptualization, Funding acquisition.

Data availability

Data will be made available on request.

Declaration of competing interest

The authors declare that they have no known competing financial interests or personal relationships that could have appeared to influence the work reported in this paper.

Acknowledgments

The work of S. Chu was supported in part by the DFG (German Research Foundation) through HE5386/19-3, 27-1. The work of A. Kurganov was supported in part by NSFC grant 12171226 and W2431004. The work of S. Mohammadian and Z. Zheng was supported by the Australian Research Council (DP240102189).

Appendix A. Generalized minmod reconstruction

In this appendix, we briefly describe a piecewise linear generalized minmod reconstruction [29–31].

Assume that the cell averages $\bar{\psi}_j$ of a certain function $\psi(x)$ are given. We use them to reconstruct a second-order piecewise linear interpolant

$$\widetilde{\psi}(x) = \bar{\psi}_j + (\psi_x)_j(x - x_j), \quad x \in C_j, \tag{A.1}$$

and then to compute the right- and left-sided point values of ψ at the cell interfaces $x = x_{j+\frac{1}{2}}$:

$$\psi^-_{j+\frac{1}{2}} = \bar{\psi}_j + \frac{\Delta x}{2}(\psi_x)_j, \quad \psi^+_{j+\frac{1}{2}} = \bar{\psi}_{j+1} - \frac{\Delta x}{2}(\psi_x)_{j+1}. \tag{A.2}$$

In order to ensure a non-oscillatory nature of this reconstruction, we compute the slopes $(\psi_x)_j$ in Eq. (A.1) using a generalized minmod limiter:

$$(\psi_x)_j = \text{minmod}\left(\theta\,\frac{\bar{\psi}_j - \bar{\psi}_{j-1}}{\Delta x}, \frac{\bar{\psi}_{j+1} - \bar{\psi}_{j-1}}{2\Delta x}, \theta\,\frac{\bar{\psi}_{j+1} - \bar{\psi}_j}{\Delta x}\right), \quad \theta \in [1, 2], \tag{A.3}$$

where the minmod function is defined as

$$\text{minmod}(z_1, z_2, \ldots) := \begin{cases} \min_j\{z_j\} & \text{if } z_j > 0 \quad \forall\, j, \\ \max_j\{z_j\} & \text{if } z_j < 0 \quad \forall\, j, \\ 0 & \text{otherwise.} \end{cases} \tag{A.4}$$

The parameter θ in Eq. (A.3) can be used to control the oscillations: larger θ's correspond to sharper but, in general, more oscillatory reconstructions.

Appendix B. Local characteristic decomposition

In order to suppress the oscillations in the piecewise linear reconstruction of ρ and q inside the congested domain, we apply the generalized minmod limiter from Appendix A to the local characteristic variables. To this end, we first introduce the matrix

$$\widehat{A}_{j+\frac{1}{2}} = A(\widehat{\boldsymbol{U}}_{j+\frac{1}{2}}) = \begin{pmatrix} -\dfrac{\widehat{q}_{j+\frac{1}{2}}}{\rho_{\max}} & \dfrac{\rho_{\max} - \widehat{\rho}_{j+\frac{1}{2}}}{\rho_{\max}} \\ \dfrac{\widehat{q}_{j+\frac{1}{2}}(q^* - \widehat{q}_{j+\frac{1}{2}})}{\widehat{\rho}^2_{j+\frac{1}{2}}} & \dfrac{(q^* - 2\widehat{q}_{j+\frac{1}{2}})(\widehat{\rho}_{j+\frac{1}{2}} - \rho_{\max})}{\widehat{\rho}_{j+\frac{1}{2}}\rho_{\max}} \end{pmatrix}, \tag{B.1}$$

where $A = \frac{\partial \boldsymbol{F}}{\partial \boldsymbol{U}}$, $\widehat{\rho}_{j+\frac{1}{2}} = \frac{\bar{\rho}_j + \bar{\rho}_{j+1}}{2}$ and $\widehat{q}_{j+\frac{1}{2}} = \frac{\bar{q}_j + \bar{q}_{j+1}}{2}$, and construct the following matrix, which consists of the two eigenvectors of $\widehat{A}_{j+\frac{1}{2}}$:

$$R_{j+\frac{1}{2}} = \begin{pmatrix} \dfrac{\widehat{\rho}_{j+\frac{1}{2}}}{\widehat{q}_{j+\frac{1}{2}} - q^*} & \dfrac{\widehat{\rho}_{j+\frac{1}{2}}(\rho_{\max} - \widehat{\rho}_{j+\frac{1}{2}})}{\widehat{q}_{j+\frac{1}{2}}\rho_{\max}} \\ 1 & 1 \end{pmatrix}. \tag{B.2}$$

We then compute its inverse

$$R^{-1}_{j+\frac{1}{2}} = \begin{pmatrix} \dfrac{\widehat{q}_{j+\frac{1}{2}}(\widehat{q}_{j+\frac{1}{2}} - q^*)\rho_{\max}}{\widehat{\rho}_{j+\frac{1}{2}}(\widehat{q}_{j+\frac{1}{2}}\widehat{\rho}_{j+\frac{1}{2}} + q^*(\rho_{\max} - \widehat{\rho}_{j+\frac{1}{2}}))} & \dfrac{(\widehat{q}_{j+\frac{1}{2}} - q^*)(\widehat{\rho}_{j+\frac{1}{2}} - \rho_{\max})}{\widehat{q}_{j+\frac{1}{2}}\widehat{\rho}_{j+\frac{1}{2}} + q^*(\rho_{\max} - \widehat{\rho}_{j+\frac{1}{2}})} \\ \dfrac{\widehat{q}_{j+\frac{1}{2}}(q^* - \widehat{q}_{j+\frac{1}{2}})\rho_{\max}}{\widehat{\rho}_{j+\frac{1}{2}}(\widehat{q}_{j+\frac{1}{2}}\widehat{\rho}_{j+\frac{1}{2}} + q^*(\rho_{\max} - \widehat{\rho}_{j+\frac{1}{2}}))} & \dfrac{\widehat{q}_{j+\frac{1}{2}}\rho_{\max}}{\widehat{q}_{j+\frac{1}{2}}\widehat{\rho}_{j+\frac{1}{2}} + q^*(\rho_{\max} - \widehat{\rho}_{j+\frac{1}{2}})} \end{pmatrix}, \tag{B.3}$$

and introduce the local characteristic variables $\boldsymbol{\Gamma}$ in the neighborhood of $x = x_{j+\frac{1}{2}}$:

$$\boldsymbol{\Gamma}_k = R^{-1}_{j+\frac{1}{2}}\,\overline{\boldsymbol{U}}_k, \quad k = j-1, j, j+1, j+2. \tag{B.4}$$

Finally, we compute the slopes $(\boldsymbol{\Gamma}_x)_j$ using the generalized minmod limiter Eq. (A.3) applied to $\boldsymbol{\Gamma}$ in a componentwise manner, evaluate the point values of $\boldsymbol{\Gamma}$:

$$\boldsymbol{\Gamma}^-_{j+\frac{1}{2}} = \boldsymbol{\Gamma}_j + \frac{\Delta x}{2}(\boldsymbol{\Gamma}_x)_j \quad \text{and} \quad \boldsymbol{\Gamma}^+_{j+\frac{1}{2}} = \boldsymbol{\Gamma}_{j+1} - \frac{\Delta x}{2}(\boldsymbol{\Gamma}_x)_{j+1}, \tag{B.5}$$

and end up with obtaining the corresponding point values of $\boldsymbol{U}$:

$$\boldsymbol{U}^\pm_{j+\frac{1}{2}} = R_{j+\frac{1}{2}}\boldsymbol{\Gamma}^\pm_{j+\frac{1}{2}}. \tag{B.6}$$

References

[1] S. Mohammadian, Z. Zheng, M. Md, A. Haque, A. Bhaskar, Performance of continuum models for realworld traffic flows: comprehensive benchmarking, Transport. Res. B Meth. 147 (2021) 132–167.
[2] S. Mohammadian, Z. Zheng, M. Md, A. Haque, A. Bhaskar, Continuum modeling of freeway traffic flows: state-of-the-art, challenges and future directions in the era of connected and automated vehicles, Commun. Transp. Res. 3 (2023) 100107. Paper No.
[3] Y. Qian, J. Zeng, N. Wang, J. Zhang, B. Wang, A traffic flow model considering influence of car-following and its echo characteristics, Nonlinear Dyn. 89 (2017) 1099–1109.
[4] J. Zeng, Y. Qian, J. Li, Y. Zhang, D. Xu, Congestion and Energy Consumption of Heterogeneous Traffic Flow Mixed with Intelligent Connected Vehicles and Platoons, 2023, p. 609.
[5] J. Zeng, Y. Qian, F. Yin, L. Zhu, D. Xu, A multi-value cellular automata model for multi-lane traffic flow under lagrange coordinate, Comput. Math. Organ. Th. 28 (2022) 178–192.
[6] J. Zhang, Y. Qian, J. Zeng, X. Wei, H. Li, Hybrid Characteristics of Heterogeneous Traffic Flow Mixed with Electric Vehicles Considering the Amplitude of Acceleration and Deceleration, 2023, p. 614. Paper No 128556.
[7] C. Daganzo, Requiem for second-order fluid approximations of traffic flow, Transport. Res. B Meth. 29 (1995) 277–286.
[8] M. Treiber, A. Kesting, D. Helbing, Three-phase traffic theory and two-phase models with a fundamental diagram in the light of empirical stylized facts, Transport. Res. B Meth. 44 (2010) 983–1000.
[9] B.S. Kerner, Failure of classical traffic flow theories: stochastic highway capacity and automatic driving, Phys. A 450 (2016) 700–747.
[10] R.M. Colombo, A 2×2 hyperbolic traffic flow model, Math. Comput. Modell. 35 (2002) 141–163.
[11] S. Blandin, D.B. Work, P. Goatin, B. Piccoli, A.M. Bayen, A general phase transition model for vehicular traffic, SIAM J. Appl. Math. 71 (2011) 107–127.
[12] R.M. Colombo, M. Garavello, Phase transition model for traffic at a junction, J. Math. Sci. 196 (2014) 30–36.
[13] S. Blandin, J. Argote, A.M. Bayen, D.B. Work, Phase transition model of non-stationary traffic flow: definition, properties and solution method, Transport. Res. Part B Meth. 52 (2013) 31–55.
[14] R.M. Colombo, Hyperbolic phase transitions in traffic flow, SIAM J. Appl. Math. 63 (2002) 708–721.
[15] C. Chalons, P. Goatin, Godunov scheme and sampling technique for computing phase transitions in traffic flow modeling, Interface. Free. Bound. 10 (2008) 197–221.
[16] A. Kuganov, S. Noelle, G. Petrova, Semidiscrete central-upwind schemes for hyperbolic conservation laws and Hamilton-Jacobi equations, SIAM J. Sci. Comput. 23 (2001) 707–740.
[17] A. Kurganov, C.-T. Lin, On the reduction of numerical dissipation in central-upwind schemes, Commun. Comput. Phys. 2 (2007) 141–163.
[18] A. Kurganov, E. Tadmor, New high-resolution semi-discrete central schemes for hamilton-Jacobi equations, J. Comput. Phys. 160 (2000) 720–742.
[19] A. Chertock, S. Chu, M. Herty, A. Kurganov, M. Lukáčová-Medviďová, Local Characteristic Decomposition Based Central-Upwind Scheme, 2023, p. 473. Paper No 111718.
[20] S. Chu, A. Kurganov, R. Xin, New Low-dissipation Central-upwind Schemes. Part II, 2025, p. 103. Paper No 33.
[21] A. Kurganov, R. Xin, New Low-dissipation Central-upwind Schemes, 2023, p. 96. Paper No 56.
[22] W.S. Don, D.-M. Li, Z. Gao, B.-S. Wang, A Characteristic-wise Alternative WENO-Z Finite Difference Scheme for Solving the Compressible Multicomponent Non-reactive Flows in the Overestimated Quasi-conservative Form, 2020, p. 82. Paper No 27.
[23] T. Nonomura, K. Fujii, Characteristic finite-difference WENO scheme for multicomponent compressible fluid analysis: overestimated quasi-conservative formulation maintaining equilibriums of velocity, pressure, and temperature, J. Comput. Phys. 340 (2017) 358–388.
[24] J. Qiu, C.-W. Shu, On the construction, comparison, and local characteristic decomposition for high-order central WENO schemes, J. Comput. Phys. 183 (2002) 187–209.
[25] C.-W. Shu, Essentially non-oscillatory and weighted essentially non-oscillatory schemes, Acta Numer. 5 (2020) 701–762.
[26] S. Gottlieb, D. Ketcheson, C.-W. Shu, Strong Stability Preserving Runge-Kutta and Multistep time Discretizations, World Scientific Publishing Co Pte. Ltd, Hackensack, NJ, Hackensack, NJ, 2011.
[27] S. Gottlieb, C.-W. Shu, E. Tadmor, Strong stability-preserving high-order time discretization methods, SIAM Rev. 43 (2001) 89–112.
[28] S. Chu, A. Kurganov, S. Mohammadian, Z. Zheng, Fifth-order A-WENO path-conservative central-upwind scheme for behavioral non-equilibrium traffic models, Commun. Comput. Phys. 33 (2023) 692–732.
[29] K.-A. Lie, S. Noelle, On the artificial compression method for second-order nonoscillatory central difference schemes for systems of conservation laws, SIAM J. Sci. Comput. 24 (2003) 1157–1174.
[30] H. Nessyahu, E. Tadmor, Nonoscillatory central differencing for hyperbolic conservation laws, J. Comput. Phys. 87 (1990) 408–463.
[31] P.K. Sweby, High resolution schemes using flux limiters for hyperbolic conservation laws, SIAM J. Numer. Anal. 21 (1984) 995–1011.